XX IMEKO World Congress
Metrology for Green Growth
September 9–14, 2012, Busan, Republic of Korea

MODELLING AND ANALYSIS OF NOVEL COIL DESIGN FOR BIOMEDICAL IMPLANTED DEVICES

Imran M. Khan[1], Mokhaled M. Mohammed, Sheroz Khan[2] , Othman O. Khalifa[3]
Department of Electrical and Computer Engineering,
Faculty of Engineering, International Islamic University Malaysia
Kuala Lumpur, Malaysia
[1]imranmoezkhan@gmail.com, [2]sheroz@iium.edu.my, [3]khalifa@iium.edu.my

Abstract: Inductive coupling has been the focus of attention over recent years for powering implantable devices. This paper focuses on developing a model for a novel coil design that takes the form of Figure-8 geometry. Two different mathematical models are developed and verified with simulation results in a Finite Element Method (FEM) computational electromagnetic simulator. Circuit parameters of the coil pair are extracted and the resonant primary and secondary tanks are designed.

Keywords: biomedical implants, wireless power transfer, inductive coupling.

1. INTRODUCTION

Continuous parameter monitoring for patients with critical ailments is of paramount importance in the medical field. Similar to the way passive RFID tags are powered; inductive coupling can allow an external source to provide energy to implanted biomedical sensors [1]. One coil of appropriate size and dimension is attached to the implanted device, and the other coil is used on a system that is either wearable or mountable, carrying an external reader [2]. There is a flurry of similar research activity taking place in the field of industrial automation, electric vehicle charging and functional stimulating of organs in the field of bio-medical sciences [3-5].

Although convenient, inductive coupling carries with it challenges such as coils misalignment that significantly decreases the transmitted power and leads to very weak received signal.

There is evidence from studies in Transcranial Magnetic Stimulation (TMS) [6] that Figure-8 shaped coils form a useful magnetic flux pattern that can be used for stimulating neurons in the brain. However, these coils have not been explored in the context of powering implanted devices. In this paper, a novel coil design in the form of a Figure-8 shaped geometry is suggested as a transmit coil, and two different coil models are developed and assessed for their accuracy. This paper is organized as follows: Section 2 presents the novel coil design; Section 3 develops a mathematical model based on first principles; Section 4 compares the developed models with FEM simulation of the geometry; Section 5 gives details of the inductive link; Section 6 concludes.

2. NOVEL FIGURE-8 COIL DESIGN

A Figure-8 can be ideally thought of as two circles in one plane, intersecting at a tangent to each other at a certain point as shown in Fig. 1.

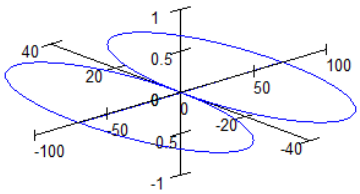

Fig. 1: Ideal Figure-8 geometry.

However, this idealized geometry fails to take into account the height and number of winding turns necessary for an actual coil. A real Figure-8 coil that can be fabricated is shown in Fig. 2 and Fig. 3.

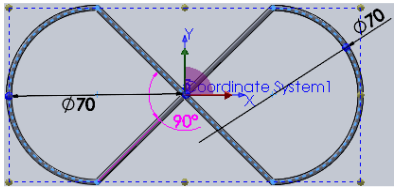

Fig. 2: Planar view of Figure-8 coil.

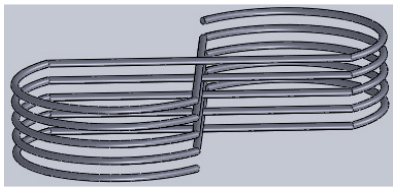

Fig. 3: Isometric view of Figure-8 coil.

It can be discerned from these figures that the coil consists of two semicircles whose centres are two radii apart, and are connected by straight wires that crossover each other. Little work has been done in the modelling of Figure-8 shaped coils especially under lateral misalignment. The

following section develops a generalized model based on two families of curves.

3. MATHEMATICAL MODELING

A numeral 8-shaped coil can be modelled by two different analytical parametric curves: Lemniscate of Bernoulli and a Lissajous Curve. The primary purpose in developing an analytical model is to show how lateral misalignment will affect the performance of the system in terms of signal and power transfer between the coils.

3.1 Lemniscate of Bernoulli

The Lemniscate of Bernoulli is a curve defined parametrically in equations (1-3), where a represents the foci, h is the height of the coil and n is the number of turns.

The curve is graphed in Fig. 4 in two dimenions.

$$x(t) = \frac{a\sqrt{2}\cos(t)}{\sin^2(t)+1} \tag{1}$$

$$y(t) = \frac{a\sqrt{2}\cos(t)\sin(t)}{\sin^2(t)+1} \tag{2}$$

$$z(t) = \frac{h}{2\pi n}t \tag{3}$$

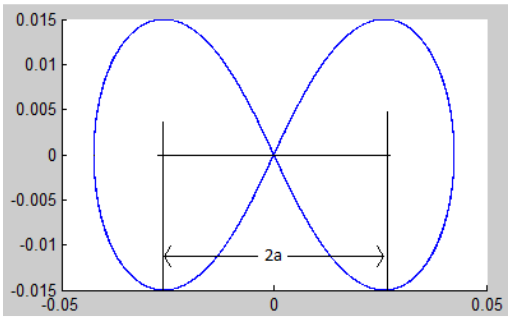

Fig. 4: Lemniscate of Bernoulli

The parametric derivatives of the curve are given in equations (4-6).

$$x'(t) = \frac{-a\sqrt{2}\sin(t)(\sin^2(t)+1) - 2a\sqrt{2}\sin(t)\cos^2(t)}{(\sin^2(t)+1)^2} \tag{4}$$

$$y'(t) = \frac{(a\sqrt{2}\cos^2(t) - a\sqrt{2}\sin^2(t))(\sin^2(t)+1) - 2a\sqrt{2}\sin(t)\cos^2(t)}{(\sin^2(t)+1)^2} \tag{5}$$

$$z'(t) = \frac{h}{2\pi n} \tag{6}$$

3.2 Lissajous Curve

The other curve considered in this paper for modelling a numeral 8-shaped coil is a Lissajous curve. This is defined parametrically as shown in the equations in (7-9), where a is a parameter defining the foci, h is the height of the coil and n is the number of turns.

The curve is graphed in Fig. 5 in two dimensions.

$$x(t) = a\cos(t) \tag{7}$$

$$y(t) = a\sin(2t) \tag{8}$$

$$z(t) = \frac{h}{2\pi n}t \tag{9}$$

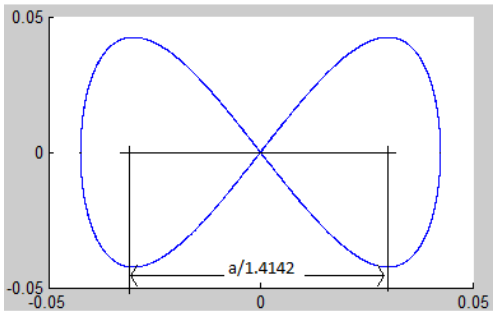

Fig. 5: Lissajous curve

The parametric derivatives of the curve are given in equations (10-12).

$$x'(t) = -a\sin(t) \tag{10}$$

$$y'(t) = 2a\cos(2t) \tag{11}$$

$$z'(t) = \frac{h}{2\pi n} \tag{12}$$

Although both curves define a rough figure-8, they are quite dissimilar in shape (Fig. 6).

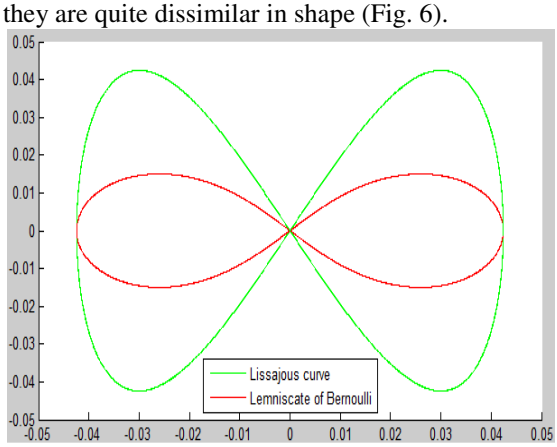

Fig. 6: Curves for Figure-8 coil model.

The basic principle of inductive coupling is quite old and well-established. It is principally governed by the Biot-Savart Law as in equation (13).

$$\vec{B} = \frac{\mu I}{4\pi}\int \frac{d\vec{l}\times\vec{m}}{\|m\|^3} \tag{13}$$

In the case that the primary and secondary coils are laterally misaligned as shown in Fig. 7, it is important to solve the Bio-Savart Law in terms of the misalignment.

For any curve that is defined parametrically by a vector l, and is displaced in space by Δx, Δy and d in the direction of the displacement vector m, it is

possible to give the definitions of the vectors required in Biot-Savart's Law as shown in equations (14-16), and the length of the distance vector as shown in equation (17).

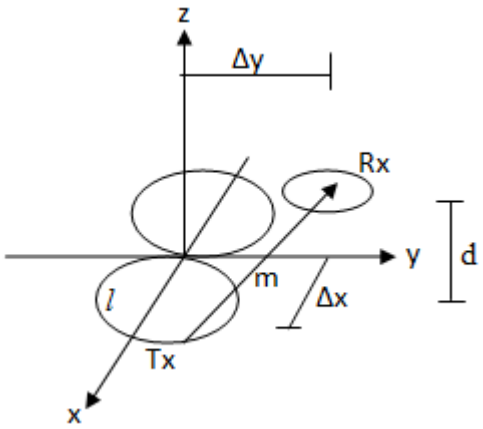

Fig. 7: Laterally displaced coils.

$$\vec{l} = \langle x(t), y(t), z(t) \rangle \tag{14}$$

$$d\vec{l} = \langle x'(t), y'(t), z'(t) \rangle \tag{15}$$

$$\vec{m} = \langle \Delta_x - x(t), \Delta_y - y(t), d - z(t) \rangle \tag{16}$$

$$\|m\| = \sqrt{[\Delta_x - x(t)]^2 + [\Delta_y - y(t)]^2 + [d - z(t)]^2} \tag{17}$$

Solving the Biot-Savart Law for the general magnetic field components, equations (18-20) can be obtained and solved numerically for the different components of the magnetic field.

$$\vec{B}_x = \frac{\mu I}{4\pi} \int_0^{2\pi} \frac{y'(t)[d - z(t)] - z'(t)[\Delta_y - y(t)]}{\|m\|^3} dt \tag{18}$$

$$\vec{B}_y = \frac{\mu I}{4\pi} \int_0^{2\pi} \frac{x'(t)[z(t) - d] + z'(t)[\Delta_x - x(t)]}{\|m\|^3} dt \tag{19}$$

$$\vec{B}_z = \frac{\mu I}{4\pi} \int_0^{2\pi} \frac{x'(t)[\Delta_y - y(t)] - y'(t)[\Delta_x - x(t)]}{\|m\|^3} dt \tag{20}$$

These developed models are tested against an FEM computational electromagnetic simulation developed in the COMSOL 4.0 Multi-physics suite.

4. FEM SIMULATION RESULTS

The geometries of the primary and secondary coils were designed in Dssault Systeme's SolidWork CAD software and imported into COMSOL 4.0 Multiphysics Suite. The dimensions of the primary and secondary coils are given in Table 1.

The Figure-8 shaped coil was excited by a 1A current at one terminal at 100kHz frequency, and had a secondary coil in the shape of solenoid nearby. In Fig. 8, a focused flux pattern can be seen to be generated around the coil that clearly shows flux lines passing through the two lobes of the Figure-8 shaped coil.

Table 1. Dimensions of primary and secondary coils.

	Primary	Secondary
Radius (mm)	35 (lobe)	20
Wire diameter (mm)	2	2
Height (mm)	20	10
Number of turns	5	3
Inter-turn distance (mm)	2	3

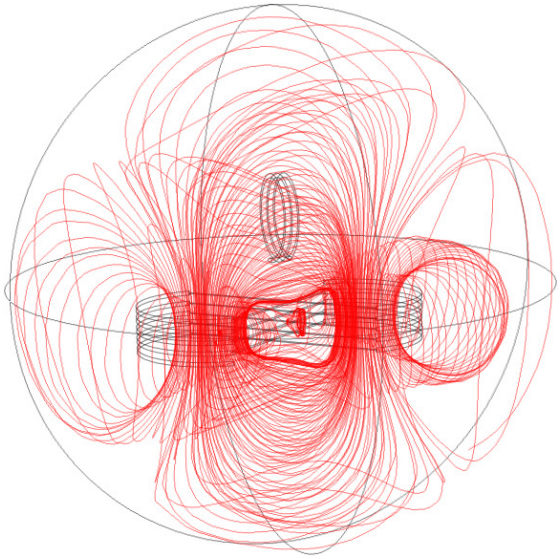

Fig. 8: Flux pattern for Figure-8 coil.

This is an intuitive flux pattern when considering that the two lobes behave like two spiral coils, with oppositely oriented currents. The flux lines seem to focus in the x-direction near the centre of the coils as expected. These points of intensities of flux lines prove to be good locations for the position of secondary coil intended in this telemetric system as shown in Fig. 8.

The lateral misalignment effects of both the models are compared to the simulation results and shown in Fig. 9. The flux pattern intensity is calculated along the line define by the intersection of the planes x=0mm and z=40mm. This is an appropriate distance to consider as most near-surface implants are placed in the 30-50mm range beneath the skin.

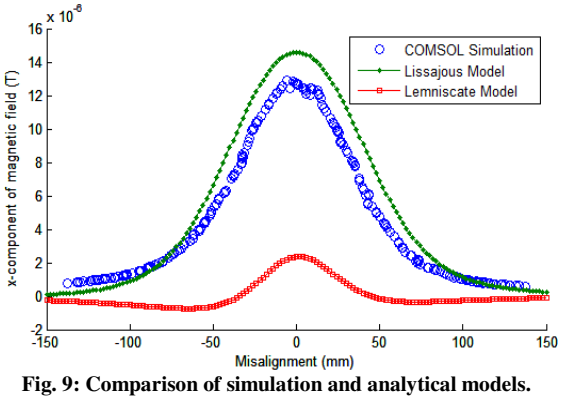

Fig. 9: Comparison of simulation and analytical models.

It can be clearly seen from Fig. 9 that the Lissajous curve model is more accurate than the Lemniscate model. Additionally, it can be seen that although the wire is only 3mm in diameter, the magnetic field remains substantially unaltered at even 20mm away from the centre.

The Figure-8 coil was also compared with spiral and solenoid coils which have been designed to be electromagnetically similar to the Figure-8 coil and have been modelled and described in [7]. The relevant components of the magnetic field intensities of the coils are shown in Fig. 10, where misalignment is considered to be along the y-axis at the intersections of the planes x=0mm and z=20mm.

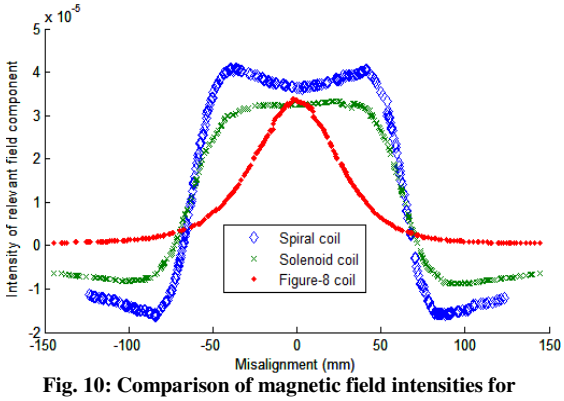

Fig. 10: Comparison of magnetic field intensities for different coil shapes.

It can be seen from Fig. 10 that the Figure-8 coil provides magnetic field intensity comparable to the solenoid and spiral coils. Although the field is more focused, it decays more gradually with misalignment as compared to the sudden drop in field intensity in the case of the solenoid and spiral. Furthermore, the Figure-8 coil seems more stable than the spiral coil which exhibits a slight drop in intensity near its centre. Additionally, the peak value of the magnetic field intensity of the Figure-8 coil is slightly higher than that of the solenoid.

The variation of the mutual inductance between the primary and secondary coils is given in Fig. 11.

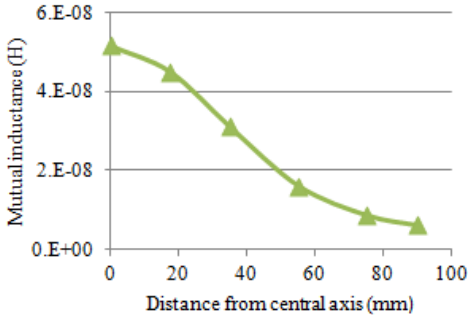

Fig. 11: Mutual inductance variation with misalignment.

The maximum value of the mutual inductance is when there is no misalignment between the primary and secondary coils and has a value of 0.05nH.

5. INDUCTIVE LINK DESIGN

The circuit level parameters of inductance and AC Equivalent Series Resistance (ESR) for both the primary and secondary coils can be extracted from the FEM simulation and are given in Table 2.

Table 2. Coil circuit parameters.

	Inductance (µH)	AC ESR (Ω)
Primary	3.62	0.0558
Secondary	0.512	0.0101

Due to the very low coupling achieved between the primary and secondary coil (k≈0.04) it is necessary to have resonance in the primary and secondary sides of the inductive link circuit.

Series resonance can be achieved simply by including a series capacitor on the secondary side of the circuit as shown in Fig. 12, where R_1 is a source resistance chosen to be 10Ω; R_2 and R_3 are the ESR of the primary and secondary coils respectively; and R_4 is a load resistor of 0.01Ω representing a sensor or transducer, specifically chosen to be of nearly equivalent value to the ESR of the secondary coil.

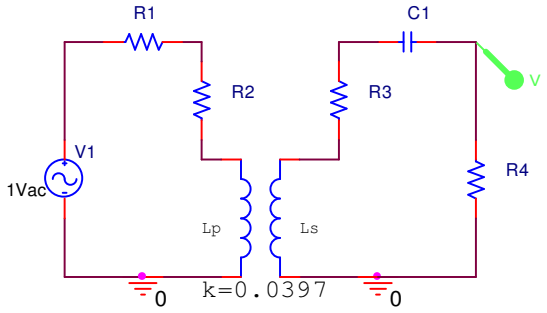

Fig. 12: Inductive link circuit.

The value of the secondary capacitor C_1=4.9472µF, is calculated as shown in equation (21) where L_s is the secondary inductance; and f_o is the desired operating frequency, which in this case is 100kHz.

$$C_1 = \frac{1}{4\pi^2 f_o^{\,2} L_s} \qquad (21)$$

The frequency response of the circuit shown in Fig. 13 displays resonance at 100kHz, with a maximum of the voltage transfer function of 1.62mV.

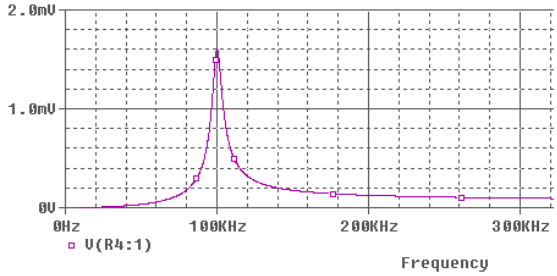

Fig. 13: Inductive link frequency response.

It should be recognized that instability of the power transfer during normal operation of the inductive link is caused by two factors: variation in the mutual inductance due to coil misalignment and variation in the value of the sensor (load) element. Although most works on the topic do not consider the influence of these effects, it is worthwhile to analyze the impact of these variations on the total transfer function as they affect the stability of the inductive link.

The transfer function for the inductive link (given in Fig. 12) is shown under variation of mutual inductance (given in Fig. 11) and load resistance (R_4) in Fig. 14.

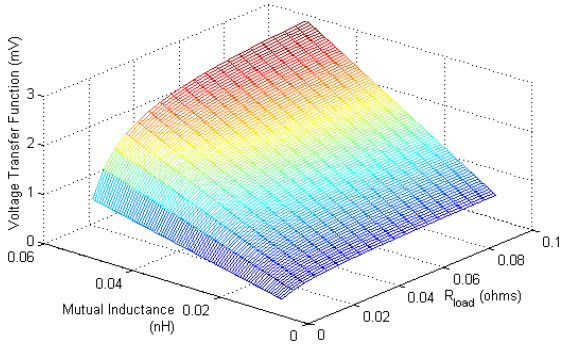

Fig. 14: Transfer function with variation of mutual inductance and load resistance.

Fig. 14 shows that the expected voltage transferred between the primary and secondary side is in the low millivolt ranges. Furthermore, it can be seen that the effect of the mutual inductance is mostly linear, especially at higher values of the load resistor. Also, the value of the load resistance plays a greater role when the mutual inductance between the coils is higher. Thus, it can be concluded that for a secondary series-resonant topology, not only is alignment of the primary and secondary coils important for maximum power transfer, but also a stable and linear sensor element should be chosen.

6. CONCLUSION

This paper has presented a novel coil design in the form of Figure-8 shape. Two different mathematical models are developed and verified with their simulation counterpart results using an FEM computational electromagnetic simulator. It is found that the Lissajous curve model predicts more accurately the actual magnetic field intensity under misalignment for the Figure-8 geometry considered in this paper. The Figure-8 coil is also compared with usual geometries of solenoid and spiral coils. Variations in mutual inductance due to misalignment between the Figure-8 primary coil and a solenoid secondary coil are also given. Circuit-level parameters of the primary and secondary coil pair are extracted from the FEM simulation and a secondary series-resonant inductive link circuit is designed that operates at 100kHz. The effect of variation in mutual inductance and variation of sensor (load) element value on the voltage transfer function is studied and some conclusions are drawn about the secondary series-resonant inductive link topology. The simulation results are highly encouraging, achieving voltage transfer in the low millivolt ranges.

Future direction of on-going work will look into other promising applications of implantable devices such precise rectification and clock recovery.

7. REFERENCES

[1]. N. F. Guler and E. D. Beyli, "Theory and Applications of Biotelemetry," Journal of Medical Systems, Vol. 26, No. 2, pp. 159-178, April 2002.

[2]. R. Puers, K. Van Schuylenbergh, Inductive Powering: Basic Theory and Application to Biomedical Systems. Springer, Ch. 2, pp. 42-50, 2009.

[3]. U.K. Madawala and D.J. Thrimawithana, "A Bi-Directional Inductive Power Interface for Electric Vehicles in V2G Systems," IEEE Transactions on Industrial Electronics, Vol. 58, No. 10, pp. 4789-4796, Oct. 2011.

[4]. P. Si, A. P. Hu, S. Malpas and D. Budgett, "A Frequency Control Method for Regulating Wireless Power to Implantable Devices," IEEE Transactions on Biomedical Circuits and Systems, Vol. 2, No. 1, pp. 22-29, March 2008.

[5]. S. Y. Lee, C. H. Hsieh and C. M. Yang, "Wireless Front-End with Power Management for an Implantable Cardiac Micro-stimulator," IEEE Transactions on Biomedical Circuits and Systems, Vol. 6, No. 1, pp. 28 – 38, Jan. 2012.

[6]. G. Xu, Y. Chen, S. Yang, M. Wang and W. Yan, "The optimal design of magnetic coil in transcranial magnetic stimulation," In Proc. 27th Annual IEEE Conference of Engineering in Medicine and Biology, pp. 6221-6224, 2005.

[7]. I. M. Khan, S. Khan and O. O. Khalifa, "Wireless Transfer of Power to Low-Power Implanted Biomedical Devices: Coil Design Considerations," In Proc. IEEE International Instrumentation and Measurement Technology Conference (I2MTC), pp. 2584-2588, 2012.